Analyst

Dynamic Article Links ►

Cite this: DOI: 10.1039/c0xx00000x

www.rsc.org/xxxxxx

PAPER

Subcellular Spectroscopic Markers, Topography and Nanomechanics of Human Lung Cancer and Breast Cancer Cells Examined by Combined Confocal Raman microspectroscopy and Atomic Force Microscopy

Gerald D. McEwen [†, a], Yangzhe Wu [†, a, ϕ], Mingjie Tang [a], Xiaojun Qi [b], Zhongmiao Xiao [b], Sherry M. Baker [c], Tian Yu [c], Timothy A. Gilbertson [c], Daryll B. DeWald [c, Δ], Anhong Zhou [*, a]

Received (in XXX, XXX) Xth XXXXXXXXX 20XX, Accepted Xth XXXXXXXXX 20XX
DOI: 10.1039/b000000x

Nanostructures and hydrophobic properties of cancer cell membranes are important in based on membrane fusion and cell adhesion. These are directly related to cancer cell biophysical properties, including, aggressive growth and migration. Additionally, chemical component analysis of the cancer cell membrane could potentially be applied in clinical diagnosis of cancer by identification of specific biomarker receptors expressed on cancer cell surfaces. In the present work, a combined Raman microspectroscopy (RM) and atomic force microscopy (AFM) technique was applied to detect the difference in membrane chemical components and nanomechanics of three cancer cell lines; human lung adenocarcinoma epithelial cells (A549), and human breast cancer cells (MDA-MB-435 with and without BRMS1 metastasis suppressor). Raman spectral analysis indicated similar bands between the A549,435 and 435/BRMS1 including ~720 cm^{-1} (guanine band of DNA), 940 cm^{-1} (skeletal mode polysaccharide), 1006 cm^{-1} (symmetric ring breathing phenylalanine), and 1451 cm^{-1} (CH deformation). The membrane surface adhesion forces for these cancer cells were measured by AFM in culture medium: 0.478±0.091 nN for A549 cells, 0.253±0.070 nN for 435 cells, and 1.114±0.281 nN for 435/BRMS1 cells, and the cell spring constant was measured at 2.62±0.682 mN/m for A549 cells, 2.105±0.691 mN/m for 435 cells, and 5.448±1.081 mN/m for 435/BRMS1 cells.

Introduction

The mechanical properties of cells play a fundamental role in the regulation of cell structures and functions, such as intracellular and/or intercellular forces sensing and transmitting, biochemical signals transducing and generating cellular responses [1]. The mechanical properties (including adhesion, elasticity and stiffness) of cancer cells have been recognized as a contributing factor in cellular adherence, mobility, transformation, invasion, and metastasis [2]. It is known that the mechanical properties, cell topography, membrane surface nanostructures, and cellular biochemical components change among different cancer cell lines, and these differences are connected to the development of new clinical diagnostic approaches [2-5]. Therefore, it is of importance to characterize these cellular differences at the single cell and sub-cellular level. However, this type of characterization remains largely uninvestigated due to the lack of applicable technologies that can reach nanoscale resolutions. The development and application of atomic force microscopy (AFM) and Raman microspectroscopy provide new access to cell mechanics, cytoarchitectures, and biochemical components of cancer cells [2-8] at the single cell and sub-cellular levels.

Breast Cancer Metastasis Suppressor 1 (BRMS1) gene

It has been shown that breast cancer metastasis suppressor 1 (BRMS1) gene can suppress the formation of metastasis without affecting orthotopic tumor growth [9], and BRMS1 expression in breast adenocarcinoma cells (MDA-MB-435) can be restored using microcell mediated chromosome transfer and thus result in suppression of metastasis [10, 11]. However, it is unclear how BRMS1-expression could alter cell topographical structures, membrane surface nanostructures, cytoskeleton, cell mechanics and cellular biochemical compositions; nor, how these biophysical and biochemical parameters for MDA-MB-435 cells differ from those of other cancer cell line like A549 cells (human lung adenocarcinoma epithelial cell line). Knowledge of these differences could facilitate new applications of AFM and Raman for early diagnosis of human cancers.

Raman Microspectroscopy

Raman microspectroscopy (RM) is a nondestructive vibrational classification routine that can be utilized to identify characteristic spectroscopic fingerprints of living cells based on chemical compositions and molecular structures [12]. Briefly, Raman spectral frequencies are recorded in wavenumber units which are proportional to vibrational energies based on molecular polarizability [13]. Many former RM studies focused mainly on

physical and structural investigations. Over the past few decades, due to advances within instrumentation design [14, 15], biological applications [16, 17], and methods for biochemical information extraction [18, 19], RM has exhibited increased popularity in the field of mammalian cell biology [7, 20]. Short *et al.* demonstrated the use of RM to detect biochemical changes, in tumorogenic versus nontumorogenic cells, as a result of proliferation [21]. More recently, Abramczyk *et al.* reported the hallmarks of normal, malignant, benign breast tissue characterized by Raman studies [22]. Several other studies reported the appearance of cellular biopolymers (including DNA/RNA, lipids, proteins, and carbohydrates) in cell growth [7, 19, 23]. As RM has increased in popularity, new analysis routines have emerged to extract useful chemical composition information from Raman spectra. Advances have been made to obtain Raman scattering from inherent background fluorescence through automation [24, 25], while other groups move toward an automated pre- and post-processing routine to eliminate natural user variability [26] and categorize Raman spectra [27]. Also new and emerging methods have been explored to enhance the usefulness of Raman spectral maps/images. Principal component analysis (PCA) was used to evaluate maps of freeze dried and living cells [28]. Gardner *et al.* has shown the usefulness of loading plot analysis to differentiate PC-3 from MGH-U1 cells using a 514.5 nm laser [29]. Ling *et al.* demonstrated image-processing algorithms to restore Raman image degradation in the study of anticancer drug distribution within living cells [12]. When key molecular components are used, RM becomes a powerful tool for rapid characterization of normal and transformed breast epithelial cell-lines [7] and multivariate analysis classification models can discriminate normal from abnormal tissue in cervical cancer progression [19]. Popp *et al.* has performed extensive work with multivariate algorithms to analyze single cells with Raman and discusses advantages and disadvantages of spatial information extraction [30].

Atomic Force Microscopy

Previously, AFM had been widely used in cell biology studying, because it can simultaneously obtain surface structures and mechanics of cells [2, 5, 31]. This has allowed researchers to better understand the relationship between cell functions and biophysical alterations, such as to assess the biophysical alterations of mammalian cells associated with functional gene expressing or oncogenic transformation. Until now, there are only a few AFM applications in cancer cell line studies, which revealed that cancerous cells are largely softer and less adhesive [2, 3] and have a lower Young's modulus [8, 32] compared to normal/benign cells. This work and others [4, 5, 31, 32] demonstrate the importance of AFM detection of nano-biomechanics and the potential for early cancer diagnosis.

Our aim in this study was to assess the usefulness of combining AFM/Raman technologies to distinguish differences in cellular biochemical markers, topography, membrane nanostructures and mechanics, among the following cancer cell lines; human lung adenocarcinoma epithelial cells (A549), metastatic human breast carcinoma cells MDA-MB-435 (435) and non-metastatic MDA-MB-435/BRMS1 (435/BRMS1). This study has selected to understand potential fundamental links between biochemical makeup, cytoarchitectural, and biomechanical changes among various cancer cell lines. Our results showed that A549 cells possessed a rougher cell membrane, and larger adhesion force and cell elasticity than 435 cells, and that BRMS1-expression increased membrane surface roughness, adhesion force and cell elasticity in 435/BRMS1 cells. To our knowledge, this was the first work to use both Raman microspectroscopy and AFM to investigate biochemical and biophysical differences of two cancer cell lines. This work suggested that the potential of applying a combined Raman and AFM approach can reveal more information to study the association of cell biochemical composition and biomechanics of cancer cells.

Materials and Methods

Preparation of human breast cancer cell line 435 and 435/BRMS1 and human lung adenocarcinoma cell A549

435/BRMS1 cells were transfected with a lentiviral vector construct expressing full length BRMS1 cDNA under the control of a cytomegalovirus promoter. 435 and 435/BRMS1 cells were cultured in a 1:1 mixture of Dulbecco's-modified eagle's medium (DMEM) and Ham's F-12 medium supplemented with 5% fetal bovine serum (Hyclone, Logan, UT). Cells were cultured in 25-cm^2 Corning tissue culture dishes at 37 °C with 5% CO_2 in a humidified atmosphere. Cells were passaged at 80-90% confluency using 2 mM EDTA in $Ca^{2+/}Mg^{2+}$-free phosphate buffered saline (PBS, 0.01 M, pH 7.4, Thermo Scientific). Cell lines were confirmed to be free of mycoplasma contamination using PCR (TaKaRa, Japan). No antibiotics or antimycotics were used in either cell cultures.

Human (Homo sapiens) lung carcinoma A549 cells (ATCC, USA) were cultured in F-12k medium containing 10% fetal bovine serum at 37°C with 5% CO_2 in a humidified atmosphere. Cells were passaged at 80-90% confluency and used for experiments. No antibiotics or antimycotics were used in cell cultures.

Confocal Raman Microspectroscopy

Raman spectra were acquired using a Renishaw inVia Raman spectrometer (controlled by WiRE 3.0 software) connected to a DMLM Leica microscope (Leica, Germany). The Raman spectrometer was equipped with a 785 nm near-IR laser (laser spot 10 × 3 μm line) that was focused through a 63 × NA = 0.90 water immersion objective (Leica, Germany). The spectrometer was calibrated with silicon at a static spectrum centered at 520.5 cm^{-1} for 1 second. Each cell line, A549, 435, and 435/BRMS1 were cultured in quartz dishes to 80-90% confluency, then mounted on the microscope stage and imaged. Spectra were collected in static mode and pinhole setting for 1 accumulation at 10 seconds laser exposure over a wavenumber range of 500 – 1800 cm^{-1} for cells and background at the same focal plane [33]. The purpose of using the pinhole and narrowing the range of the illuminated area of the cells was to reduce the amount of the background artifact. Five spectra were used to obtain an average for each cell line and background. Averaged background spectra were subtracted from averaged cell line spectra by finding a local minimum area (GRAMS/AI 8.0, Thermo Electron Corp., USA). Each spectrum was baseline corrected (Vancouver Raman Algorithm) [25], then normalized using peak intensity at 1450 cm^{-1} [34], which represents a CH deformation that is not significantly

affected by intercellular changes [33]. Raman spectral maps were collected in a "StreamLine" mode for 30 seconds exposure time at wavenumber center 910 cm^{-1}. If necessary, Cosmic Ray Removal (CRR) was performed and signal-to-baseline intensity was analyzed.

Chemometic analysis of Raman spectra and spectral images

Firstly, moving average smoothing pre-processing was done to the Raman spectra to filter high-frequency noise. Then, second derivative of smoothed spectra was performed to eliminate baseline drifts and background interference. This pre-treatment is often used to distinguish overlapping peaks and improve resolution and sensitivity of spectra [35-37]. The Raman spectra were analyzed by principal components analysis (PCA) to extract information from raw spectral data and eliminate much overlapped information, and then an unsupervised Ward's hierarchical cluster analysis (HCA) with Euclidean distances [38] was performed to qualitatively distinguish the differences among three cell lines. All algorithms were implemented in Matlab R2010b (Mathworks, Natick, USA).

PCA was employed to analyze Raman spectra for single cell Raman images. The detailed steps to obtain PC1 (the 1st principal component) and PC2 (the 2nd principal component) score images for the single cell Raman spectral image, which was corrected for cosmic rays and smoothed, are as follows.

The spectral data of each single cell was read and arranged into matrix A, whose width is the number of cells in the spectral image and whose height is the length of the spectral data in each cell. Then the covariance matrix U was computed according to equation 1.

$$U = \frac{1}{M}\sum_{i=1}^{M}\left[A_i - \mu\right] * \left[A_i - \mu\right]^T \qquad \text{Eqn 1}$$

Where μ is the average spectra data of all cells in the image, M is the number of cells in the image, and A_i corresponds to the i^{th} column in A (i.e., the spectral data of the i^{th} cell). Eigenvalues and eigenvectors of the covariance matrix U were computed and eigenvalues were sorted in descending order and eigenvectors were reorganized in matrix D, where $D = [D_1\ D_2\ \ldots\ D_n]$ with D_i corresponding to the eigenvector of the i^{th} largest eigenvalue and n being the number of distinct eigenvalues. The PC1 scores were computed (i.e., projected values in the first PC direction) by multiplying D_1^T by $A - \mu$ and rearranging the PC1 scores to the corresponding cells in the PC1 score image. Similarly, PC2 scores (i.e., projected values in the second PC direction) were computed by multiplying D_2^T by $A - \mu$ and rearranging the PC2 scores to the corresponding cells in the PC2 score image.

For AFM experiments, cells were seeded on poly-L-lysine coated Petri dishes at 5×10^4 cells/mL. The same seeding density was used for Raman spectroscopy; only cells were seeded in quartz dishes (Quartz Scientific Inc., 313R020, USA) to minimize background artifacts.

Atomic Force Microscopy

In order to image viable carcinoma cells *in vitro* via AFM, two sample preparation approaches were utilized: 1) live cells were measured directly in culture medium without any pretreatment to record in situ measurements of biomechanical properties (e.g. adhesion behavior, cellular spring constant), or 2) to visualize fixed cells instead of mechanics measurment, the cells were pretreated by fixative 1% glutaraldehyde plus 1% paraformaldehyde dissolved in 1 × $Ca^{2+/}Mg^{2+}$-free phosphate buffered saline for 5 minutes, followed by gentle rinsing using PBS, and then, the cells were imaged in PBS.

The contact mode PicoPlus AFM controlled by PicoScan 5.4 software (Picoplus, Agilent Technologies, USA) was used to measure cells at 22 ~ 25 °C in PBS (0.01 M, pH 7.4) (for fixed cells) or directly in cell culture medium (for live cells). The spring constant of the cantilever was calibrated at 0.06 ~ 0.11 N/m (Veeco, USA) with tip length between 0.4 ~ 0.7 μm, and Si_3N_4 tip curvature radius of approximately 10 nm. The approach/retract velocity applied throughout deflection (nm) vs. distance (nm) curve acquiring was 6.1 μm/second. The values for the adhesion force (the detachment force between bare AFM tip and cell membrane in the process of AFM cantilever retracting) were extracted from the deflection (nm) vs. distance (nm) curves via the Scanning Probe Image Processor (SPIP) software (Image Metrology, Denmark). The compliance slope portion of the deflection-distance curves was used to evaluate the cellular spring constants (k_{cell}), which were calculated using a previously proposed formula [39, 40],

$$k_{cell} = -k_{tip} \cdot \frac{s}{1+s} \qquad \text{Eqn 2}$$

Where, s is the linear slope of the approaching branch, the ratio of *deflection (nm)* to *distance (nm)*; k_{cell} and k_{tip} represent the spring constants of cell and cantilever, respectively.

In addition, the average roughness (R_a) and root-mean-square roughness (R_{rms}) were obtained according to equation 3 and 4 [41]:

$$R_a = \frac{1}{N} \cdot \sum_{n=1}^{N} \left| z_n - \bar{z} \right| \qquad \text{Eqn 3}$$

$$R_{rms} = \sqrt{\frac{\sum_{n=1}^{N} \left(z_n - \bar{z}\right)^2}{N-1}} \qquad \text{Eqn 4}$$

Where N represents the total number of data points in a selected area, z_n is the height of the n^{th} point, and $\bar{z}$ is the mean height.

Furthermore, to assess statistically significant differences in nano-mechanics including adhesion force and cellular elasticity among these cancer cell lines, the data were reported as mean±s.d. (standard deviation of mean), and analyzed using Student's t-test. The data used to graph histograms or created force maps were measured from the whole cell body, and the histograms were drawn using OriginPro 7.5 (OriginLab Corp., USA). The adhesion force or cellular spring constant maps were graphed with as 256 color maps created by Matlab R2010b (Mathworks, Natick, USA).

RESULTS/DISCUSSION

Raman spectral analysis - Biochemical markers of three cell lines

In this study, RM was utilized as a method to characterize cellular biochemical composition for each cancer cell line; A549, 435 and 435/BRMS1. Fig. 1 is a stacked view of the averaged raw data for A549, 435, 435/BRMS1, and the quartz/culture medium background, respectively (offset vertically for clarity).

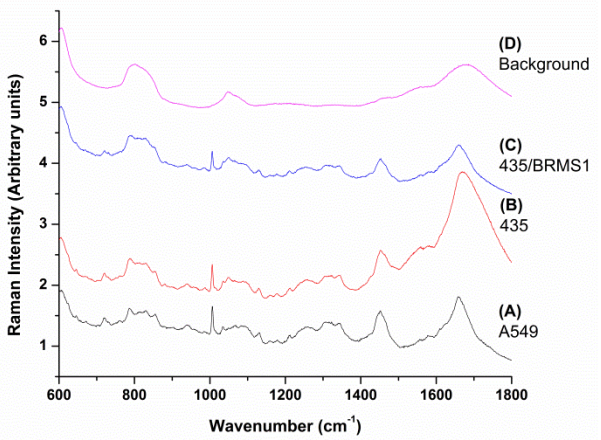

Fig.1 Averaged Raman spectra for three cancer cell lines and background, respectively: A549 (**A**-black), 435 (**B**-red), 435/BRMS1 (**C**-blue), and background (**D**-magenta). For each cell line the Raman spectrum represent an average of five separate spectra and the background is an average of fifteen spectra. Spectra are offset vertically for clarity.

To better understand the differences between each cell line, the Raman spectra were post-processed as previously described (section 2.2). Fig.2 depicts stacked Raman spectra normalized at 1450 cm^{-1}. These spectra exhibit minor differences, which are probably minimized based on the semi-confocal probing approach of the cellular regions. The post-processing procedure assists to reveal subtle variations among each spectrum, yet maintain similarities for spectra of the same cell type.

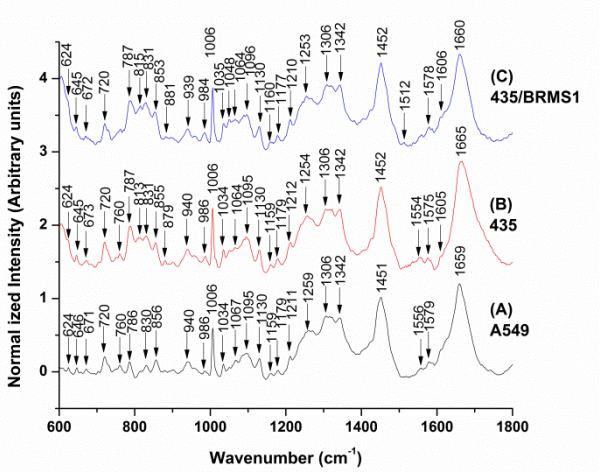

Fig. 2 Mean Raman spectra of three cancer cell lines: A549 (**A**-black), 435 (**B**-red), and 435/BRMS1 (**C**-blue). Each spectrum is the average of five spectra, the averaged background was subtracted by finding a local minimum area, spectra were baseline corrected, and then normalized using peak intensity at 1450 cm^{-1}. Spectra are offset vertically for clarity.

Mean RM spectra are illustrated in Fig. S2 with only minor variations based on the selected normalization band represented. In the 1450 cm^{-1} normalized Fig. 2, the overall spectral fingerprint for A549, 435 and 435/BRMS1, are very similar. However, initial background in Fig. 2B,C obscure the 624 cm^{-1} (protein) band of 435 and 435/BRMS1, another likely background artifact is present between ~770 – 872 and 1023 – 1148 cm^{-1}, which could be caused by the quartz substrate. Further, a very weak shoulder peak at 1606 cm^{-1} (protein) is visible for both 435 and 435/BRMS1 and the Amide I band at 1660 cm^{-1} for 435 is blue shifted from ~1660 to 1665 cm^{-1}. On the other hand, the 813 cm^{-1} (one of two RNA bands) is missing in Fig. 2A for A549 along with the previously mentioned background artifacts.

In Fig. S1 (Supplemental materials), normalized at 1660 cm^{-1}, the same spectral difference are noted that were described for Fig. S2 with relative intensity changes based on the ratio of the 1450 to 1660 cm^{-1} Raman bands.

Additionally, data mining is required to extract useful biochemical information to further compare each cell line. The first step is to assign various vibrational modes to each mean spectrum to provide a primary level of understanding. Tentative Raman bands are listed in Table 1.

Table 1 Tentative Raman band assignments for human lung adenocarcinoma epithelial cell (A549) and human metastatic (435) and non-metastatic (435/BRMS1) breast carcinoma cells

Raman shift (cm^{-1})			**Band assignment**
A549	435	435/BRMS1	
624			Phenylalanine
646	645	645	C-C twist Phenylalanine
671	672	672	
720	720	720	DNA
760	760		Tryptophan
786	788	787	DNA & phosphdiester bands DNA
	813	814	Phosphodiester bands RNA
830	830	829	PO_2^- stretch nucleic acids
856	855	853	Tyrosine
	880		Tryptophan
940	940	939	Skeletal modes (polysaccharides)
984	986	984	
1006	1006	1006	Phenylalanine
1034	1034	1035	Phenylalanine
		1050	
1066			PO_2^- stretching (DNA/RNA); chain stretching (lipids); C-O, C-C stretching (carbohydrates)
1095	1095	1096	Lipid
1130	1129	1129	C-C skeletal stretch transconformation
1160	1160		
1179	1178	1178	Cytosine, guanine
1211	1211	1211	Tyrosine, phenylalanine
1259	1255	1254	Lipid; A,T breathing mode (DNA/RNA); Amide III (protein)
1306	1306	1308	C-N stretching aromatic amines
1343	1342	1342	G (DNA/RNA); CH deformation (proteins and carbohydrates)
1451	1452	1452	CH_2 deformation (nucleic acid, proteins, lipids)
	1553		
1579	1575	1579	Pyrimidine ring (nucleic acids)
1659	1666	1660	Amide I

[a] Band assignments are based on [7, 42]

An approach that is somewhat better than direct comparison (as in Fig. 2 and Fig. S1) is to compute difference spectra by subtracting one mean normalized spectrum from another [34, 43]. Fig. 3 and Fig. S2 are the computed difference spectra from Figs. 2 and Fig. S1, respectively.

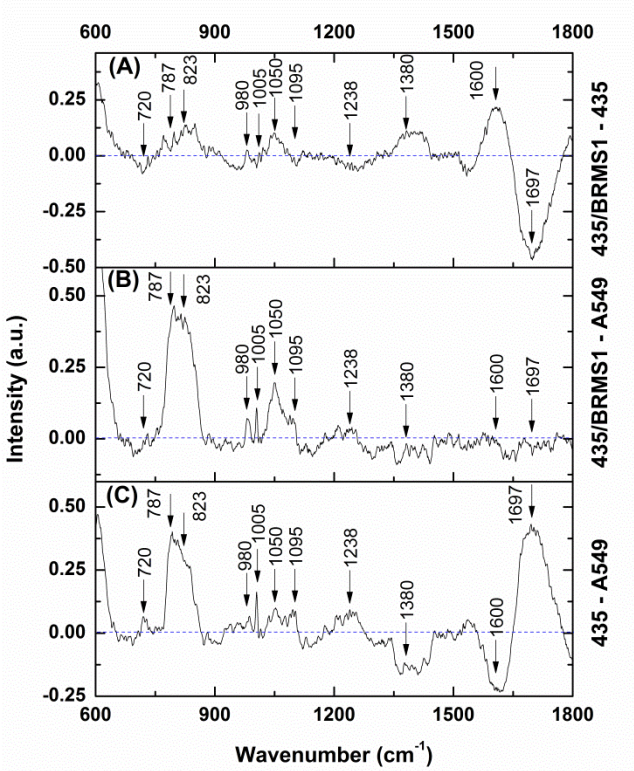

Fig.3 Difference spectra computed from the 1450 cm^{-1} normalized spectrum in Fig. 2 using A549, 435, and 435/BRMS1: 435/BRMS1 – A549 (**A**); 435/BRMS1 – A549 (**B**); A549 – 435 (**C**).

PCA was performed on the post-processed data as shown in Fig. 2 and the score plot (also known as the loading plot) of the first three principal components is shown in Fig. 4. It should be noted that the same post-processing techniques, namely, the baseline correction and the normalization technique, are applied on three cell lines to ensure the background information is removed and the three cell-lines are compared from the spectral perspectives. Due to the specific acquisition parameters used for the Raman system, we were able to acquire 29 spectra (9 spectra for A549, 9 spectra for 435, 11 spectra for 435/BRMS1). In the score plot, each sample is represented by a single point and the origin of the graph is the data set average. The x-axis, labeled PC1, is the score values for the first principal component; the y-axis, PC2, the second principal component, and the z-axis, PC3, the third principal component. The samples are color coded according to the sample type. The score plot demonstrates the three cells samples are distinguishable into three distinct groups. Even though our data sample set is relatively small, the three clusters clearly show the grouping effect of each cell type and the similarity within each cell type and the dissimilarity across different cell types.

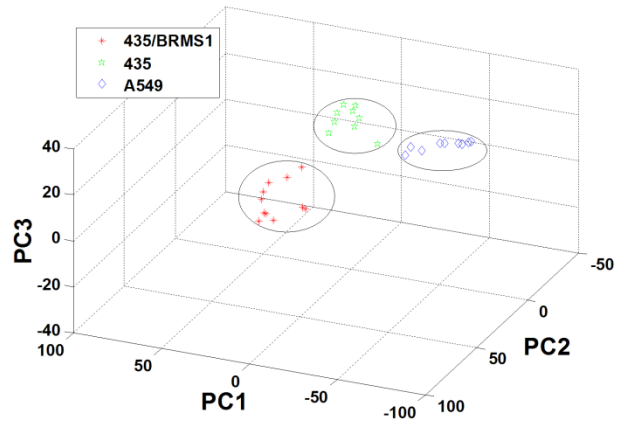

Fig. 4 PCA score plot for pre-processed Raman spectra for each cell line. Each cancer cell line is coded by color and shape (435/BRMS1 - red star, 435 - green pentagram, and A549 - blue diamond).

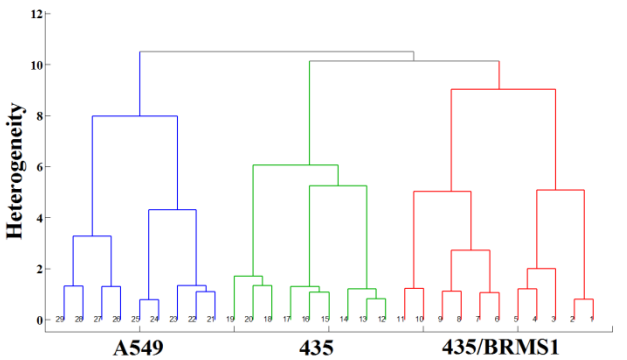

Fig. 5 Dendogram analysis based on PCA score values for the first six principal components. The data is color coded into three groups. By including six PCs, the dendogram shows that the spectral data can be correctly categorized according to cancer cell line type.

Fig. 5 shows the dendrogram resulting from HCA performed on a total of 29 spectra (9 spectra for A549, 9 spectra for 435, 11 spectra for 435/BRMS1). The first six principal components were used as the input parameters, which account for 97.2% of the variation in the data set. The dendrogram was generated using Ward's clustering algorithm and the squared Euclidean distance. The Euclidean distance method is a simple approach for the classification of multivariate data. In Fig. 5, the horizontal axis stands for the labeling of the 29 cells, and the vertical axis represents the heterogeneity (or dissimilarity) distance between two cells or cluster. Apparently, the 29 spectra (or cells) formed three separated clusters, one per cell type. The dendrogram shows that the Raman spectra of these three cell lines can be grouped, regardless the 435/BRMS1 and 435 cell lines are much more similar to each other than the A549 cell line.

Raman spectral image analysis - Biochemical markers of three cell lines

Figs. 6A-C represent white light images for A549, 435, and 435/BRMS1 along with overlaid spectral maps for specific Raman bands which correspond to biochemical components of interest: DNA (Fig. 6D-F), carbohydrate (Fig. 6G-I), protein (Fig. 6J-L), and lipid (Fig. 6M-O). Characteristic Raman band intensity analysis provides spectral maps or images with spatial and temporal distribution for major biochemical components at single

or sub-cellular levels.

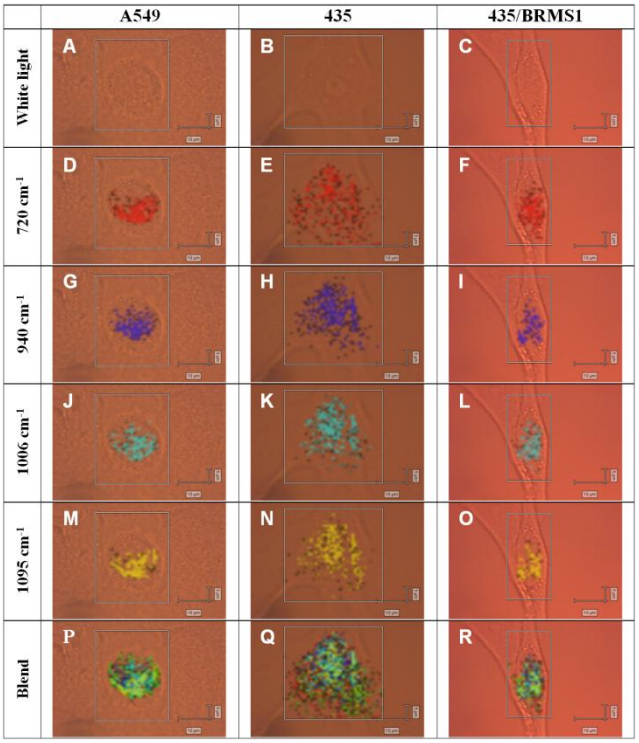

Fig.6 Raman spectral images for relative biochemical distribution within single cells; A549, 435 and 435/BRMS1. White light images (A-C). Different biochemical components were identified by characteristic wavenumber as follows; DNA (D-F, red) – 720 cm^{-1}, carbohydrate (G-I, blue) – 940 cm^{-1}, protein (J-L, cyan) – 1006 cm^{-1}, and lipid (M-O, yellow) – 1095 cm^{-1}. Complete biochemical distribution overlays (P-R). Scale bar: 10 µm (horizontal), 5 µm (vertical).

Fig. 7 represents the PC1 and PC2 score images for three single cell Raman images. Here, PC1 and PC2 score images account for the two most significant PC components and show the summary of variations at all wavenumbers used in the PCA. Each score image shows a separate variation that is linearly independent of the other score image. Specifically, PC1 and PC2 score images contain the largest and the second largest variation among all the choices of the PC component, respectively.

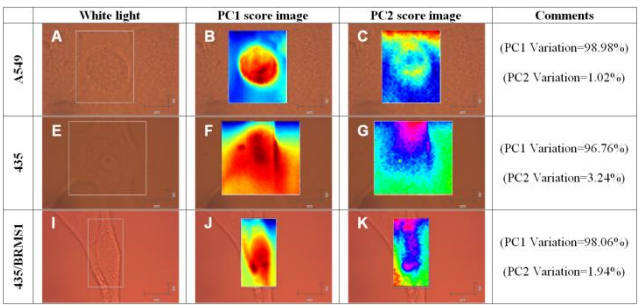

Fig. 7 Single cell Raman spectral image maps for A549, 435, 435/BRMS1: first column (white image), 2nd column (PC1 score image), 3rd column (PC2 score image). The colors were scaled for butter visualization and displaying purpose. Scale bar: 10 µm (horizontal), 5 µm (vertical).

AFM observation of cell membrane nanostructure

To assess the differences in cell topography and cell membrane surface nanostructures among each cancer cell line, fixed cells were imaged by contact mode AFM in PBS, and the results are shown in Fig. 8. The 1st column gives the representative images of single A549 and 435 cells and multiple 435/BRMS1 cells. The 2nd column shows their respective deflection mode images. The 3rd and 4th columns show the nanostructures of the cellular membrane at two different locations for each individual cell type.

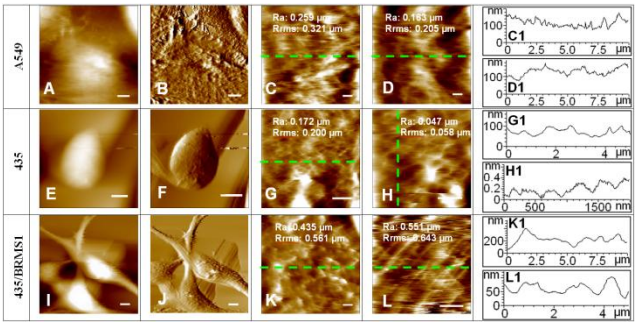

Fig.8 Topography and membrane surface nanostructures of A549, 435, and 435/BRMS1 acquired in PBS. The 1st column shows the topography images; 2nd column the respective deflection images, 3rd and 4th columns show the membrane surface nanostructures (roughness values marked) obtained at two different locations for each cell line. The 5th column presents the cross section profiles taken along the green dash lines. Scale bar: 5 µm (A,B,E,F,I,J), 1 µm (C,D,G,K,L), 500 nm (H).

AFM Measurements of nanomechanical properties of cancer cell lines

Different cellular topography and membrane surface structures could alter cellular mechanics, for example, cellular elasticity and adhesion. To further evaluate the nanomechanical differences among each cell line, the adhesion interaction force (F) between the bare AFM tip and the cellular membrane surface cellular spring constant (kcell), and Young's modulus (E) were analyzed based on hundreds of force-distance curves for each cell type by employing SPIP software (Sneddon cone model was selected from SPIP model channel to perform analyses). These force-distance curves were acquired using AFM contact mode in culture media and the measured results are shown in Fig. 9. Columns 1, 2 and 3 present a representative AFM image and the corresponding nanomechanical results (row 2, F maps and histograms; row 3, kcell maps and histograms; row 4, E maps and histograms) of A549, 435, and 435/BRMS1, respectively. The low resolution images in Fig. 9 (row 1) may be resulted from the very soft cell membrane (evidenced by the low cellular spring constants as shown in Fig. 9, row 3) and the presence and movement of membrane surface microvillus of living cells during tip scanning. Therefore, we mainly focused on the acquisition of deflection (nm) vs distance (nm) curve to evaluate the nano-biomechanics of living cells.

The parametric statistical analysis (Student's t-test) indicated that the adhesion force, cell spring constant and Young's modulus measured among three cell lines were significantly different ($p < 0.01$). To clearly illustrate the variations of these three parameters, the statistical data (mean±s.d.) were marked on their respective histograms (Fig. 9- rows 2-4).

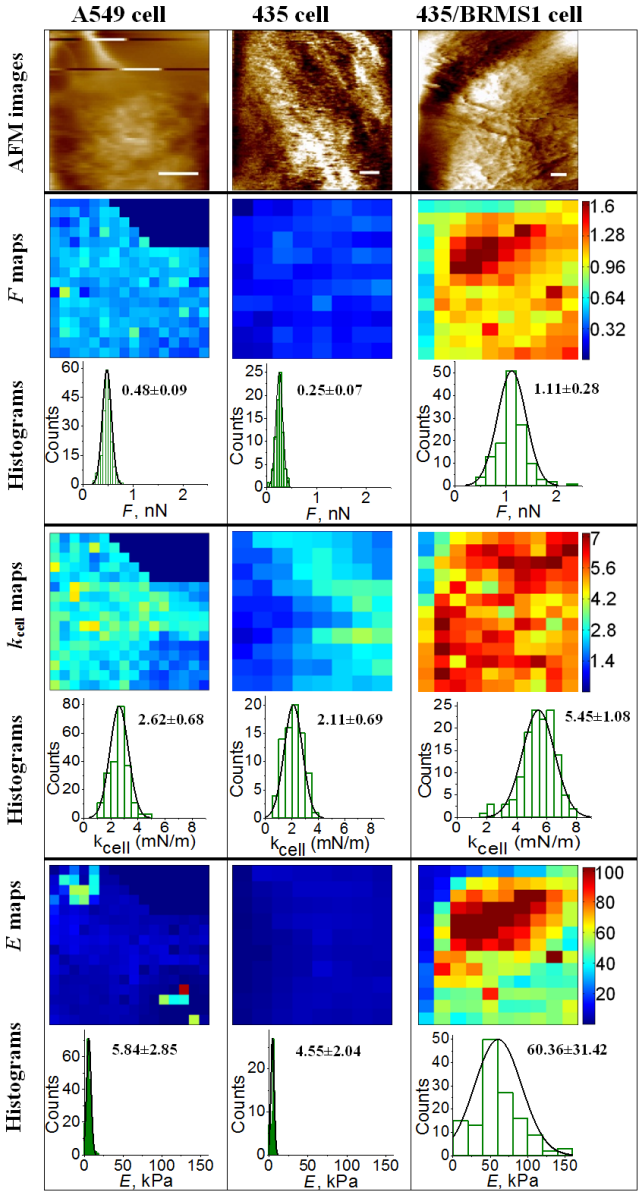

Fig.9 Biomechanical evaluation of living lung cancer cell line A549 (column 1), breast carcinoma cell lines 435 (column 2) and 435/BRMS1 cells (column 3). Row 1 shows representative topography images acquired in culture medium. The maps of adhesion force (F), spring constant (k_{cell}), and Young's modulus (E) of three cell lines are shown in row 2, row 3, and row 4, respectively, and their respective distribution histogram (mean±SD is marked) is displayed under the corresponding map. The color bars arranged at the right of maps illustrate the value scale of color-coded maps of F (nN), k_{cell} (mN/m), and E (kPa). Scale bar: 5 μm (A549 cell), 1 μm (435 cell and 435/BRMS1 cell).

Discussion

Qualitative and quantitative analysis of cell adhesion and elasticity of human cancer cells could advance the fundamental understanding of the biochemical and biomechanical developmental roles in cancer metastasis mechanisms. This present work exhibits a combined Raman microspectroscopy and atomic force microscopy approach to evaluate biochemical and biophysical properties of cellular membrane and nano-architectures, of three different model human carcinoma cells.

Raman spectral analysis - Biochemical markers of three cell lines

Raman microspectroscopy results showed that these three cell lines possess very similar biochemical components on their cell membrane surfaces, even small spectral differences could be observed from difference spectra. Gardner et al. have investigated the effect of cell size on discrimination and indicated that separation is based predominantly on cell type rather than cell size [29].

We have previously shown that both 435 and 435/BRMS1 contain similar gross biochemical compositions [44] when imaged with RM. A direct comparison, as shown in Fig. 1, does not reveal significant spectral variations among the cancer cell lines.

In order to verify if spectral difference are affected by normalization band, we also compared the normalized 1450 cm^{-1} band (Fig. 2 and Fig. 3) with another at 1660 cm^{-1} (Fig. S1 and Fig. S2). To better interpret the spectral differences and gain insight into the biochemical variation of A549, 435 and 435/BRMS1: difference spectra were computed by subtracting the metastatic spectrum from the model spectrum (435 – A549), the non-metastatic from model spectrum (435/BRMS1 – A549), and the non-metastatic from the metastatic (435/BRMS1 – 435), respectively. Differences in the spectral profiles of the breast carcinoma cells (435 and 435/BRMS1) and the lung adenocarcinoma cells (A549) were more pronounced than those from the breast carcinoma cells. This suggests that while the spectra appear to contain a similar overall fingerprint as seen in Figs. 2 and Figure S1, there are some vital distinctions that are observed. Therefore, the overall spectral fingerprint does not change based on the normalization band, only the relative intensity based on the normalization band ratio.

It was found that these cancer cell lines share many of the same characteristic Raman bands as illustrated in Table 1 and are similar biochemically although cultured using slightly different cell culture protocols (section 2.1). Based on the phase of the cell cycle, many of the cell biochemical/biopolymer components are concentrated inside living cells [45] and typical biochemical molecules of interest are associated with DNA, carbohydrates, proteins, and lipids. When measured with RS, these biochemical molecules are typically reported based on each respective Raman band assignment (also designated Raman shift, in cm^{-1}). Raman bands assignments, for the above mentioned biochemical molecules of interest, are as follows; DNA are located at ~ 720, 787, 830, 1178, and 1579 cm^{-1}, while a distinct band for carbohydrates is 940 cm^{-1}, proteins are at 1006, 1130 and 1660 cm^{-1}, and lipids are located at 1095 cm^{-1}, respectively [42]. Also, it is noted that there are bands that overlap; for example, 1066 cm^{-1} could be associated with the PO_2^- stretching of DNA/RNA, chain stretching in lipids, and C-O or C-C stretching of carbohydrates [42]; 1255 cm^{-1} may be assigned as lipid, adenine or thymine breathing modes of DNA/RNA, and the amide III band of proteins [42]; 1308 cm^{-1} might either be assigned as C-N stretching of aromatic amines [42], or CH_2 twist or bend associated with nucleic acids proteins and lipids [7]; 1342 cm^{-1} may possibly be assigned as guanine in DNA/RNA or CH deformation in proteins and carbohydrates [42]; and finally 1452 cm^{-1} could be assigned as CH_2 deformation in nucleic acids, proteins, and lipids [42]. At present, we are not able to further distinguish the overlapped

bands, yet it may be possible to use surface enhanced Raman scattering (SERS) to gain insight into the specific biochemical components of interest via a better enhanced/resolved spectra around the broad Raman bands.

In Fig. 3A, there is a two-fold decrease in the overall spectral intensity and all the negative bands, 720, 1005, 1095, 1238, and 1697 cm^{-1} are due to the 435 spectrum. The majority of these peaks can be assigned as DNA (720 – DNA, and 1095 cm^{-1} – PO_2^- in nucleic acids), proteins (1005 – phenylalanine/protein, 1238 – Amide III, and 1697 cm^{-1} – Amide I), and lipids (1095 – lipids,) with overlap in of the 1095 cm^{-1} band. The positive bands, 787, 823, 980, 1050, 1380, and 1600 cm^{-1} are from the 435/BRMS1 spectrum and can be similarly assigned; as DNA (787 – relative DNA, 823 – phosphodiester, and1095 cm^{-1} – PO_2^- in nucleic acids), proteins (980 –protein, 1602 cm^{-1} – phenylalanine/Amide I), and lipids (1380 – δ CH_3 symmetric) with no overlapping bands and one unassigned band (1050 cm^{-1}). Figs. 3B-C show a two-fold increase in the overall spectral intensity when compared with 3A. The negative bands in 3(B, C) are respectively; 1380 cm^{-1} and 1380, and 1600 cm^{-1} and were due to the A549 spectrum. Whereas the positive bands for 3(B,C) are respectively; 787, 823, 980, 1005, 1050, 1095, and 1238 cm^{-1} due to the 435/BRMS1 spectrum and 720, 787, 823, 980, 1005, 1050, 1095, 1238, and 1697 cm^{-1} due to the 435 spectrum. These peaks have been previously assigned for Fig. 3A. Difference spectra between 435/BRMS1 and 435 (Fig.S2A) yield negative bands at 720 and 1697 cm^{-1} that were due to the 435 spectrum. The positive bands; 787, 823, 980, 1005, 1050, 1095, 1238, 1380, 1441, and 1600 cm^{-1} are from the 435/BRMS1 spectrum. In Fig. S2B-C, the negative bands are respectively; 1441, 1697 cm^{-1} and 1380, 1441, and 1600 cm^{-1}; which were due to the A549 spectrum. Whereas the positive bands for Figs. S2(B-C) are respectively; 720, 787, 823, 980, 1005, 1050, 1095, 1238, and 1441 cm^{-1} due to the 435/BRMS1 spectrum, and 720, 787, 823, 980, 1005, 1050, 1095, 1238, and 1697 cm^{-1} due to the 435 spectrum. The previously mentioned background quartz artifact is visible in Figs. 3B-C and Figs. S2B-C compared to 3A and Fig. S2A.

From the difference spectra, it can be concluded that the variability within the difference spectra is associated with the differences related to the A549 spectra. This is illustrated in Fig. 3A where the spectral features less pronounced as compared with both Figs. 3B-C, which include stronger features at 787 and 823 cm^{-1} related to DNA and 1050 cm^{-1} (unassigned) and decreases at 1380 (lipid) and 1600 cm^{-1} (protein). Fig. S2A is similar to Fig. 3A and likewise Fig. S2B-C are similar to Fig. 3B-C with the exception of the addition of the Raman band at 1441 cm^{-1} (CH_2 scissoring & CH_3 bending in lipids). These slight spectral variations from the difference spectra are more insightful than Fig. 2 and Fig. S1 in that, we can now compare the relative ratios of Raman bands across each of the three cell lines. Each of the Raman band vibrational modes was assigned based on available literature [7, 42].

PCA of the pre-processed Raman spectra aid to distinguish each cell line based on cell type. Fig. 4 shows the scatter plots of the Raman spectra for these cancer cell lines projected into a three-dimensional subspace using principal component scores PC1, PC2, and PC3. It is seen that the first PC (PC1) possess 60.3% variation, PC2 19.4% variation, PC3 9.8%. Apparently, 3D PCA plots indicate that the Raman spectra of these three cell lines are distinguishable into three distinct groups – according to cancer cell line type. The intrinsic difference in biomolecular composition and concentration for different cancer cells will cause the clusters to be separated from each other. In order to better view the similarity among these three model cancer cells, hierarchical cluster analysis (HCA) was performed.

HCA is used as a nonsupervised method for obtaining information about the heterogeneity (dissimilarity) between spectra collected from different species. The dendogram (Fig. 5) shows that the three cancer cell lines can be grouped based on the heterogeneity of their spectra, indicating that breast cancer cell lines 435 and 435/BRMS1 are much more similar to each other than to lung cancer cell line A549. The two breast cancer cell lines are more biologically similar each other.

Raman spectral image analysis - Biochemical markers of three cell lines

The spectral image at band 720 cm^{-1} in Fig. 6D-F represents the guanine band distribution for DNA [42] and is concentrated centrally on the cells of A549 (Fig. 6D) and 435/BRMS1 (Fig. 6F), compared to 435 cells (Fig. 6E) where the map is more evenly spread on single cells. Raman band 940 cm^{-1} in all three cell lines (Fig. 6G-I) is assigned the skeletal mode vibrations of polysaccharides for carbohydrates [42] and these spectral image display similar distributions as in Fig. 6D,F with the similar even spread noted for 435 cells (Fig. 6E). The 1006 cm^{-1} band (Fig. 6J-L) is the symmetric ring breathing band of phenylalanine for protein [23, 42], which has a more even distribution near the center of each cell, although more broadly distributed in Fig. 6K. Finally, the 1095 cm^{-1} band (Fig. 6M-O) is the chain C-C stretch band for lipid [23], and appears to be more narrowly distributed in Fig. 6M,O and more broad in Fig. 6N. Blended images are shown in Fig. 6P-R and illustrate the overall combined biochemical distributions of these major biochemical components for A549, 435, and 435/BRMS1. Furthermore, the biochemical distributions of A549 cells are very similar those for 435/BRMS1. Both cell lines appear to have most of the biochemical components centralized at the mass of the cell. On the contrary, 435 cells seem present a broad distribution for each biochemical component. Overall, the Raman spectral images may serve as a means for rapid assessment of biochemical distribution that could be validated with traditional biology techniques, to determine cell health.

As far as PCA image analysis (Fig. 7) is concerned, all three cancer cell lines possess larger than 95% variations in the first principal component (PC1) among all the PC components. Specifically, the percentages of the variations in the first two principal components (PC1, PC2) of the spectra of these three cancer cells are: A549 (98.98%, 1.02%), 435 (96.76%, 3.24%), 435/BRMS1 (98.06%, 1.94%), respectively. As a result, the major variability of cells' Raman signals is captured in the PC1 score images, which contribute the most in the spectrum analysis of three Raman images. The figure clearly shows several distinct clusters, where different colors indicate different clusters. That is, the area with similar colors represents a cluster and indicates the spectral data of the cells have similar patterns. Three PC1 score images for three cancer cell lines demonstrate the major

variability in the data and the dark red colored areas show the most informative sampling points in their single cell Raman images.

Measurements of nanomechanical properties of cancer cell lines

The topographical images obtained in Fig. 8(B,F,J) revealed cellular morphological and structural differences of the cell surface membranes of each cell line: A549 cells exhibit a round or elliptical shape and the lamellipodia can be readily seen (Fig. 8A-B), and 435 cells also have a round or elliptical shape but no pseudopodium is seen (Fig. 8E-F); in contrast, 435/BRMS1 cells were predominately elongated (or stretched) and are long spindle-like or triangular shaped (Fig. 8I-J). Additionally, more details of membrane surface nanostructures can be observed in the 3rd and 4th columns which were obtained using a more narrow scanning area: net-like cytoskeleton structures were present on A549 cells (Fig. 8C-D) and 435 cells (Fig. 8G-H); whereas the parallel arranged cytoskeleton structures (e.g., filamentous actin) were clearly visible on 435/BRMS1 cells (Fig. 8K-L), indicating the reorganization of the cytoskeleton associated with BRMS1-expression [46]. And the cross section profiles, shown in the 5th column, further depicted the corrugation of cell membranes, suggesting non-smooth features on the cellular membrane surface. Furthermore, the quantitative comparison of membrane surface roughness (Ra and Rrms) indicated that the 435/BRMS1 cells possessed a much rougher membrane surface compared to A549 and 435 cells (the roughness values are indicated on respective image in the 3rd and 4th columns).

Fig. 9 indicates a representative AFM image and the corresponding nanomechanical results (adhesion force F maps and histograms; cell spring constant kcell maps and histograms; Young's modulus E maps and histograms) of A549, 435, and 435/BRMS1, respectively. Statistical analysis of AFM results revealed thatA549 cells had rougher cell membrane, larger cell adhesion force and cell spring constant compared to 435 cells and 435/BRMS1. The membrane surface adhesion forces for these cancer cells were measured in culture medium: 0.478±0.091 nN for A549 cells, 0.253±0.070 nN for 435 cells, and 1.114±0.281 nN for 435/BRMS1 cells, and the cell spring constant was measured at 2.62±0.682 mN/m for A549 cells, 2.105±0.691 mN/m for 435 cells, and 5.448±1.081 mN/m for 435/BRMS1 cells. These differences should be ascribed to the different cell lines that possess difference in biochemical components and biophysical properties. Meanwhile, the larger membrane adhesion force and cell elasticity for 435/BRMS1 versus 435 would have arisen from the changes in cell adhesion, cytoarchitecture and extracellular matrix in the context of BRMS1-expression [47].

Conclusions

It has been known that the adhesion motility of cancer cells is one of essential factors in the development of cancer cell metastasis [48, 49], for example, the inhibition of motility and enhancement of adhesion is very important for clinical treatment of cancer [48, 50, 51]. Therefore, the lower adhesion and a round shape may facilitate the cell movement and migration, easing the metastatic process of cancer cells; alternatively, a stronger adhesion to the substratum may make these cells too adherent (or "sticky") to migrate [48]. On the other hand, it has been reported that BRMS1 can suppress the development of metastasis without blocking orthotopic tumor growth [46, 47, 52-55] and BRMS1 expression can probably induce cytoskeleton rearrangement and alterations in cell adhesion properties [47, 52], and suppress epidermal growth factor receptor (EGFR) expression [46].

Our AFM results presented in this work revealed that BRMS1 expression in 435 cells: a) altered cell topography from round (or elliptical shape) to triangular shape; b) changed membrane cytoskeleton from net-like to parallel arrangement and thus induced a much rougher cell membrane; and c) increased membrane surface adhesion force and cell spring constant. The Raman microspectroscopy results indicated the overall similarity of the cellular surface biochemical compositions in A549, 435 and 435/BRMS1 cells, despite slightly weaker Raman band intensities that was observed in A549, the absence of the RNA band (813 cm^{-1}), and the increased amide I band (1660 cm^{-1}). These slight differences could possibly be enhanced utilizing a surface-enhanced Raman scattering (SERS) approach to gain new insight into the more subtle difference that may exist among these carcinoma cell lines. Ability to differentiate the differences in cell biochemical components and cell biomechanics between native and metastasis biomarker gene expressed (e.g., BRMS1) breast carcinoma cells would help in the determination of the biochemical and biomechanical roles of such metastasis related genes cancer cell metastasis, especially the potential relationship to extracellular matrix and cell mobility [56, 57]. The alterations in cell and sub-cellular structures, nanomechanics and biochemical components arising from BRMS1-expression are very likely to play an important role in the decrease of cell mobility and thus demonstrate its role as a metastasis suppressor. Altogether, this present work and the preliminary data revealed that the combination of atomic force microscopy and Raman microspectroscopy is a promising technique for qualitatively and quantitatively assessing the differences in cell surface structures, surface biocomponents, and cell mechanics at single cell, single molecule, and nanoscale level.

Acknowledgements

This work is partially supported by Utah Water Research Laboratory and USU Huntsman Environmental Research Center (A.Z.), USU VPR RC grant (XJQ, A.Z.), and DoD USAMRMC Breast cancer research program Grant (#W81XWH-10-1-0668) (A.Z.). The Raman microscope was acquired under a DoD Grant (#W911NF-06-01-0139) (A.Z.). G.M. thanks the support of USU Graduate Fellowship. S.B. appreciates the support of Undergraduate Research Fellowship from the Center for Integrated BioSystems at USU.

Notes and references

[a] *Department of Biological Engineering, Utah State University, Logan, Utah 84322-4105, U.S.A; E-mail: Anhong.Zhou@usu.edu*
[b] *Department of Computer Science, Utah State University, Logan, Utah 84322-4205, U.S.A*
[c] *Department of Biology, Utah State University, Logan, Utah 84322-5305, U.S.A*
† The first two authors contributed equally to this work

[φ] *Current address: Department of Microbiology and Immunology, College of Medicine, University of Illinois at Chicago, Chicago, IL 60612 USA. Email: yzwu@uic.edu*
[Δ] *Current address: Dean's Office, College of Science, Washington State University, Pullman, WA 99164-3520*

1. P. A. Janmey and C. A. McCulloch, *Annual Review of Biomedical Engineering*, 2007, 9, 1-34.
2. S. E. Cross, Y. S. Jin, J. Tondre, R. Wong, J. Rao and J. K. Gimzewski, *Nanotechnology*, 2008, 19, 384003 (384008 pp).
3. S. E. Cross, Y. S. Jin, J. Rao and J. K. Gimzewski, *Nature Nanotechnology*, 2007, 2, 780-783.
4. S. Suresh, *Nature Nanotechnology*, 2007, 2, 748-749.
5. S. Suresh, *Acta Biomaterialia*, 2007, 3, 413-438.
6. C. Kendall, M. Isabelle, F. Bazant-Hegemark, J. Hutchings, L. Orr, J. Babrah, R. Baker and N. Stone, *Analyst*, 2009, 134, 1029-1045.
7. C. Yu, E. Gestl, K. Eckert, D. Allara and J. Irudayaraj, *Cancer Detection and Prevention*, 2006, 30, 515-522.
8. Q. S. Li, G. Y. Lee, C. N. Ong and C. T. Lim, *Biochem Biophys Res Commun*, 2008, 374, 609-613.
9. L. J. Stafford, K. S. Vaidya and D. R. Welch, *Int J Biochem Cell Biol*, 2008, 40, 874-891.
10. M. J. Seraj, R. S. Samant, M. F. Verderame and D. R. Welch, *Cancer Res*, 2000, 60, 2764-2769.
11. R. S. Samant, M. J. Seraj, M. M. Saunders, T. S. Sakamaki, L. A. Shevde, J. F. Harms, T. O. Leonard, S. F. Goldberg, L. Budgeon, W. J. Meehan, C. R. Winter, N. D. Christensen, M. F. Verderame, H. J. Donahue and D. R. Welch, *Clin Exp Metastasis*, 2000, 18, 683-693.
12. J. Ling, S. D. Weitman, M. A. Miller, R. V. Moore and A. C. Bovik, *Appl. Opt.*, 2002, 41, 6006-6017.
13. D. W. Ball, *Spectroscopy*, 2001, 16, 32-34.
14. D. Pappas, B. W. Smith and J. D. Winefordner, *Talanta*, 2000, 51, 131-144.
15. P. Carey, *TrAC Trends in Analytical Chemistry*, 1983, 2, 275-277.
16. P. Hildebrandt, S. Lecomte and C. L. John, in *Encyclopedia of Spectroscopy and Spectrometry*, Elsevier, Oxford, Editon edn., 1999, pp. 88-97.
17. H. Fabian and P. Anzenbacher, *Vibrational Spectroscopy*, 1993, 4, 125-148.
18. J. R. Baena and B. Lendl, *Current Opinion in Chemical Biology*, 2004, 8, 534-539.
19. F. M. Lyng, E. Ó. Faoláin, J. Conroy, A. D. Meade, P. Knief, B. Duffy, M. B. Hunter, J. M. Byrne, P. Kelehan and H. J. Byrne, *Experimental and Molecular Pathology*, 2007, 82, 121-129.
20. C. M. Krishna, G. D. Sockalingum, G. Kegelaer, S. Rubin, V. B. Kartha and M. Manfait, *Vibrational Spectroscopy*, 2005, 38, 95-100.
21. K. W. Short, S. Carpenter, J. P. Freyer and J. R. Mourant, *Biophysical Journal*, 2005, 88, 4274-4288.
22. H. Abramczyk, J. Surmacki, B. Brozek-Pluska, Z. Morawiec and M. Tazbir, *Journal of Molecular Structure*, 2009, 924-926, 175-182.
23. I. Notingher, *Sensors*, 2007, 7, 1343-1358.
24. C. A. Lieber and A. Mahadevan-Jansen, *Appl. Spectrosc.*, 2003, 57, 1363-1367.
25. J. Zhao, H. Lui, D. I. McLean and H. Zeng, *Appl. Spectrosc.*, 2007, 61, 1225-1232.
26. F. W. L. Esmonde-White, M. V. Schulmerich, K. A. Esmonde-White and M. D. Morris, Optics in Bone Biology and Diagnostics, San Jose, CA, USA, 2009.
27. E. M. Kanter, S. Majumder, E. Vargis, A. Robichaux-Viehoever, G. J. Kanter, H. Shappell, I. Howard W. Jones and A. Mahadevan-Jansen, *Journal of Raman Spectroscopy*, 2009, 40, 205-211.
28. C. Krafft, T. Knetschke, A. Siegner, R. H. W. Funk and R. Salzer, *Vibrational Spectroscopy*, 2003, 32, 75-83.
29. T. J. Harvey, E. C. Faria, A. Henderson, E. Gazi, A. D. Ward, N. W. Clarke, M. D. Brown, R. D. Snook and P. Gardner, *Journal of Biomedical Optics*, 2008, 13, 064004.
30. M. Hedegaard, C. Matthäus, S. Hassing, C. Krafft, M. Diem and J. Popp, *Theoretical Chemistry Accounts*, 2011, 130, 1249-1260.
31. M. Lekka, P. Laidler, D. Gil, J. Lekki, Z. Stachura and A. Z. Hrynkiewicz, *European Biophysics Journal with Biophysics Letters*, 1999, 28, 312-316.
32. W. A. Lam, M. J. Rosenbluth and D. A. Fletcher, *Blood*, 2007, 109, 3505-3508.
33. G. Pyrgiotakis, T. K. Bhowmick, K. Finton, A. K. Suresh, S. G. Kane, J. R. Bellare and B. M. Moudgil, *Biopolymers*, 2008, 89, 555-564.
34. M. V. P. Chowdary, K. K. Kumar, M. Stanley, R. Lakshmi, C. M. Krishna and K. Jacob, *Biopolymers*, 2009, 91, 539-546.
35. I. T. Jolliffe, *Principal Component Analysis, 2nd edition*, 2nd edn., Springer, 2002.
36. J. M. Shaver, *Chemometrics for Raman spectroscopy. In Handbook of Raman Spectroscopy, Lewis, I. R., Edwards, H. G. M. (eds)*, Marcel Dekker, New York, 2001.
37. R. J. Barnes, M. S. Dhanoa and S. J. Lister, *Applied Spectroscopy*, 1989, 43, 772-777.
38. A. K. Jain, Dubes, R. C., ed., *Algorithms for Clustering Data*, Prentice Hall, Englewood Cliffs,NJ, 1988.
39. S. B. Velegol and B. E. Logan, *Langmuir*, 2002, 18, 5256-5262.
40. M. Arnoldi, M. Fritz, E. Bauerlein, M. Radmacher, E. Sackmann and A. Boulbitch, *Physical Review E*, 2000, 62, 1034-1044.
41. Y. Z. Wu, Y. Hu, J. Cai, S. Y. Ma, X. P. Wang and Y. Chen, *Scanning*, 2008, 30, 426-432.
42. C. Krishna, G. Sockalingum, R. Bhat, L. Venteo, P. Kushtagi, M. Pluot and M. Manfait, *Analytical and Bioanalytical Chemistry*, 2007, 387, 1649-1656.
43. Y. Wu, G. D. McEwen, S. Harihar, S. M. Baker, D. B. DeWald and A. Zhou, *Cancer Lett*, 2010, 293, 82-91.
44. E. R. Hildebrandt and N. R. Cozzarelli, *Cell*, 1995, 81, 331-340.
45. Z. Movasaghi, S. Rehman and I. U. Rehman, *Appl. Spectrosc. Rev.*, 2007, 42, 493-541.
46. K. S. Vaidya, S. Harihar, P. A. Phadke, L. J. Stafford, D. R. Hurst, D. G. Hicks, G. Casey, D. B. DeWald and D. R. Welch, *J Biol Chem*, 2008, 283, 28354-28360.
47. P. J. Champine, J. Michaelson, B. C. Weimer, D. R. Welch and D. B. DeWald, *Clin Exp Metastasis*, 2007, 24, 551-565.
48. M. T. Debies and D. R. Welch, *Journal of Mammary Gland Biology and Neoplasia*, 2001, 6, 441-451.
49. S. Zhang, Q. D. Lin and W. Di, *International Journal of Gynecological Cancer*, 2006, 16, 522-531.
50. J. M. Kirstein, K. C. Graham, L. T. MacKenzie, D. E. Johnston, L. J. Martin, A. B. Tuck, I. C. MacDonald and A. F. Chambers, *Clinical & Experimental Metastasis*, 2009, 26, 121-131.
51. L. Lu, F. Payvandi, L. Wu, L. H. Zhang, R. J. Hariri, H. W. Man, R. S. Chen, G. W. Muller, C. C. W. Hughes, D. I. Stirling, P. H. Schafer and J. B. Bartlett, *Microvascular Research*, 2009, 77, 78-86.
52. D. B. DeWald, J. Torabinejad, R. S. Samant, D. Johnston, N. Erin, J. C. Shope, Y. Xie and D. R. Welch, *Cancer Res*, 2005, 65, 713-717.
53. C. W. Rinker-Schaeffer, J. P. O'Keefe, D. R. Welch and D. Theodorescu, *Clin Cancer Res*, 2006, 12, 3882-3889.
54. L. A. Shevde and D. R. Welch, *Cancer Lett*, 2003, 198, 1-20.
55. P. S. Steeg, *Nat Rev Cancer*, 2003, 3, 55-63.
56. K. Bhadriraju and L. K. Hansen, *Exp Cell Res*, 2002, 278, 92-100.
57. D. Yamazaki, S. Kurisu and T. Takenawa, *Cancer Science*, 2005, 96, 379-386.

1. P. A. Janmey and C. A. McCulloch, *Annual Review of Biomedical Engineering*, 2007, **9**, 1-34.
2. S. E. Cross, Y. S. Jin, J. Tondre, R. Wong, J. Rao and J. K. Gimzewski, *Nanotechnology*, 2008, **19**, 384003 (384008 pp).
3. S. E. Cross, Y. S. Jin, J. Rao and J. K. Gimzewski, *Nature Nanotechnology*, 2007, **2**, 780-783.
4. S. Suresh, *Nature Nanotechnology*, 2007, **2**, 748-749.
5. S. Suresh, *Acta Biomaterialia*, 2007, **3**, 413-438.
6. C. Kendall, M. Isabelle, F. Bazant-Hegemark, J. Hutchings, L. Orr, J. Babrah, R. Baker and N. Stone, *Analyst*, 2009, **134**, 1029-1045.
7. C. Yu, E. Gestl, K. Eckert, D. Allara and J. Irudayaraj, *Cancer Detection and Prevention*, 2006, **30**, 515-522.
8. Q. S. Li, G. Y. Lee, C. N. Ong and C. T. Lim, *Biochem Biophys Res Commun*, 2008, **374**, 609-613.

9. L. J. Stafford, K. S. Vaidya and D. R. Welch, *Int J Biochem Cell Biol*, 2008, **40**, 874-891.
10. M. J. Seraj, R. S. Samant, M. F. Verderame and D. R. Welch, *Cancer Res*, 2000, **60**, 2764-2769.
11. R. S. Samant, M. J. Seraj, M. M. Saunders, T. S. Sakamaki, L. A. Shevde, J. F. Harms, T. O. Leonard, S. F. Goldberg, L. Budgeon, W. J. Meehan, C. R. Winter, N. D. Christensen, M. F. Verderame, H. J. Donahue and D. R. Welch, *Clin Exp Metastasis*, 2000, **18**, 683-693.
12. J. Ling, S. D. Weitman, M. A. Miller, R. V. Moore and A. C. Bovik, *Appl. Opt.*, 2002, **41**, 6006-6017.
13. D. W. Ball, *Spectroscopy*, 2001, **16**, 32-34.
14. D. Pappas, B. W. Smith and J. D. Winefordner, *Talanta*, 2000, **51**, 131-144.
15. P. Carey, *TrAC Trends in Analytical Chemistry*, 1983, **2**, 275-277.
16. P. Hildebrandt, S. Lecomte and C. L. John, in *Encyclopedia of Spectroscopy and Spectrometry*, Elsevier, Oxford, 1999, pp. 88-97.
17. H. Fabian and P. Anzenbacher, *Vibrational Spectroscopy*, 1993, **4**, 125-148.
18. J. R. Baena and B. Lendl, *Current Opinion in Chemical Biology*, 2004, **8**, 534-539.
19. F. M. Lyng, E. Ó. Faoláin, J. Conroy, A. D. Meade, P. Knief, B. Duffy, M. B. Hunter, J. M. Byrne, P. Kelehan and H. J. Byrne, *Experimental and Molecular Pathology*, 2007, **82**, 121-129.
20. C. M. Krishna, G. D. Sockalingum, G. Kegelaer, S. Rubin, V. B. Kartha and M. Manfait, *Vibrational Spectroscopy*, 2005, **38**, 95-100.
21. K. W. Short, S. Carpenter, J. P. Freyer and J. R. Mourant, *Biophysical Journal*, 2005, **88**, 4274-4288.
22. H. Abramczyk, J. Surmacki, B. Brozek-Pluska, Z. Morawiec and M. Tazbir, *Journal of Molecular Structure*, 2009, **924-926**, 175-182.
23. I. Notingher, *Sensors*, 2007, **7**, 1343-1358.
24. C. A. Lieber and A. Mahadevan-Jansen, *Appl. Spectrosc.*, 2003, **57**, 1363-1367.
25. J. Zhao, H. Lui, D. I. McLean and H. Zeng, *Appl. Spectrosc.*, 2007, **61**, 1225-1232.
26. F. W. L. Esmonde-White, M. V. Schulmerich, K. A. Esmonde-White and M. D. Morris, in *Optics in Bone Biology and Diagnostics*, SPIE, San Jose, CA, USA, 2009, pp. 716605-716610.
27. E. M. Kanter, S. Majumder, E. Vargis, A. Robichaux-Viehoever, G. J. Kanter, H. Shappell, I. Howard W. Jones and A. Mahadevan-Jansen, *Journal of Raman Spectroscopy*, 2009, **40**, 205-211.
28. C. Krafft, T. Knetschke, A. Siegner, R. H. W. Funk and R. Salzer, *Vibrational Spectroscopy*, 2003, **32**, 75-83.
29. T. J. Harvey, E. C. Faria, A. Henderson, E. Gazi, A. D. Ward, N. W. Clarke, M. D. Brown, R. D. Snook and P. Gardner, *Journal of Biomedical Optics*, 2008, **13**, 064004.
30. M. Hedegaard, C. Matthäus, S. Hassing, C. Krafft, M. Diem and J. Popp, *Theoretical Chemistry Accounts*, 2011, **130**, 1249-1260.
31. W. A. Lam, M. J. Rosenbluth and D. A. Fletcher, *Blood*, 2007, **109**, 3505-3508.
32. M. Lekka, P. Laidler, D. Gil, J. Lekki, Z. Stachura and A. Z. Hrynkiewicz, *European Biophysics Journal with Biophysics Letters*, 1999, **28**, 312-316.
33. G. Pyrgiotakis, T. K. Bhowmick, K. Finton, A. K. Suresh, S. G. Kane, J. R. Bellare and B. M. Moudgil, *Biopolymers*, 2008, **89**, 555-564.
34. M. V. P. Chowdary, K. K. Kumar, M. Stanley, R. Lakshmi, C. M. Krishna and K. Jacob, *Biopolymers*, 2009, **91**, 539-546.
35. I. T. Jolliffe, *Principal Component Analysis, 2nd edition*, Springer, 2002.
36. J. M. Shaver, *Chemometrics for Raman spectroscopy. In Handbook of Raman Spectroscopy, Lewis, I. R., Edwards, H. G. M. (eds)*, Marcel Dekker, New York, 2001.
37. R. J. Barnes, M. S. Dhanoa and S. J. Lister, *Applied Spectroscopy*, 1989, **43**, 772-777.
38. A. K. Jain, Dubes, R. C., ed., *Algorithms for Clustering Data*, Prentice Hall, Englewood Cliffs,NJ, 1988.
39. S. B. Velegol and B. E. Logan, *Langmuir*, 2002, **18**, 5256-5262.
40. M. Arnoldi, M. Fritz, E. Bauerlein, M. Radmacher, E. Sackmann and A. Boulbitch, *Physical Review E*, 2000, **62**, 1034-1044.
41. Y. Z. Wu, Y. Hu, J. Cai, S. Y. Ma, X. P. Wang and Y. Chen, *Scanning*, 2008, **30**, 426-432.
42. Z. Movasaghi, S. Rehman and I. U. Rehman, *Appl. Spectrosc. Rev.*, 2007, **42**, 493-541.
43. C. Krishna, G. Sockalingum, R. Bhat, L. Venteo, P. Kushtagi, M. Pluot and M. Manfait, *Analytical and Bioanalytical Chemistry*, 2007, **387**, 1649-1656.
44. Y. Wu, G. D. McEwen, S. Harihar, S. M. Baker, D. B. DeWald and A. Zhou, *Cancer Lett*, 2010, **293**, 82-91.
45. E. R. Hildebrandt and N. R. Cozzarelli, *Cell*, 1995, **81**, 331-340.
46. K. S. Vaidya, S. Harihar, P. A. Phadke, L. J. Stafford, D. R. Hurst, D. G. Hicks, G. Casey, D. B. DeWald and D. R. Welch, *J Biol Chem*, 2008, **283**, 28354-28360.
47. P. J. Champine, J. Michaelson, B. C. Weimer, D. R. Welch and D. B. DeWald, *Clin Exp Metastasis*, 2007, **24**, 551-565.
48. M. T. Debies and D. R. Welch, *Journal of Mammary Gland Biology and Neoplasia*, 2001, **6**, 441-451.
49. S. Zhang, Q. D. Lin and W. Di, *International Journal of Gynecological Cancer*, 2006, **16**, 522-531.
50. J. M. Kirstein, K. C. Graham, L. T. MacKenzie, D. E. Johnston, L. J. Martin, A. B. Tuck, I. C. MacDonald and A. F. Chambers, *Clinical & Experimental Metastasis*, 2009, **26**, 121-131.
51. L. Lu, F. Payvandi, L. Wu, L. H. Zhang, R. J. Hariri, H. W. Man, R. S. Chen, G. W. Muller, C. C. W. Hughes, D. I. Stirling, P. H. Schafer and J. B. Bartlett, *Microvascular Research*, 2009, **77**, 78-86.
52. D. B. DeWald, J. Torabinejad, R. S. Samant, D. Johnston, N. Erin, J. C. Shope, Y. Xie and D. R. Welch, *Cancer Res*, 2005, **65**, 713-717.
53. C. W. Rinker-Schaeffer, J. P. O'Keefe, D. R. Welch and D. Theodorescu, *Clin Cancer Res*, 2006, **12**, 3882-3889.
54. L. A. Shevde and D. R. Welch, *Cancer Lett*, 2003, **198**, 1-20.
55. P. S. Steeg, *Nat Rev Cancer*, 2003, **3**, 55-63.
56. K. Bhadriraju and L. K. Hansen, *Exp Cell Res*, 2002, **278**, 92-100.
57. D. Yamazaki, S. Kurisu and T. Takenawa, *Cancer Science*, 2005, **96**, 379-386.